Algebraic reconstruction of images of a diffusive medium containing strong absorbers: comparative study of different illumination schemes and the effect of restricted view angle

H. L. Graber[1], R. L. Barbour[1,2], J. Chang[2]
[1]Department of Physiology and Biophysics,
[2]Department of Pathology,
SUNY Health Science Center at Brooklyn
450 Clarkson Ave., Brooklyn, NY 11203

Abstract

The quality of the answer computed by an image reconstruction algorithm could significantly depend on certain details of the data collection and analysis procedures. We describe some of the decisions that must be taken during both of these steps, e.g., the geometry, number, and locations of both sources and detectors, selection of a set of time windows or modulation frequencies, and whether to process the data in a simultaneous or sequential manner. Because there is no set of choices is self–evidently optimal, we chose to use one comprehensive set of internal light intensity distributions and detector readings, both computed from Monte Carlo simulations, as a standard for tests of different varieties of image reconstruction algorithms applied to different subsets of detector readings. The reference medium in all cases was a densely scattering, homogeneous, infinitely long cylinder. The three targets consisted of the same cylinder with the addition of either a single black absorbing rod on the axis, a single black absorbing rod parallel to the axis, or thirteen black absorbing rods distributed in the form of an "X." Time–resolved detector responses and internal collision densities were computed directly, and from these time–independent and frequency domain data were subsequently calculated. Image were reconstructed using algebraic algorithms that solve a system of linear perturbation equations that are valid only for sufficiently weak perturbations of the reference medium. Results shown compare images obtained using data from different domains and different sets of source locations. The quality of the one–absorber images is very good to excellent. The quality of the images of the thirteen–absorber target, for which the weak perturbation premise is very strongly violated, is only fair. Sources of random and systematic errors are identified, and the effects of both types is discussed.

1. Introduction

In several publications we have shown successful image reconstructions, based on either experimental or simulated detector readings, of random media whose scattering and absorption properties are similar to those of tissue illuminated by near infrared radiation and containing either a single heterogeneity or two closely juxtaposed heterogeneities[1-4]. The algebraic techniques used seek to solve a linear perturbation equation of the form $\Delta I = \mathbf{W}\Delta x$ (1), where ΔI and Δx are, respectively, the changes in detector readings and interior optical properties of the target medium with respect to a reference medium, and each element of $\mathbf{W}$ is the constant of proportionality relating a small perturbation at one particular site in the interior to the corresponding change in the signal received by a specific detector. The formula for calculation of a weight function for a given problem depends on the illumination scheme used (i.e., steady–state (cw), time domain, frequency domain), the optical property being imaged (e.g., absorption, scattering, or transport cross section), and whether the detectors receive re–emitted incident light or light generated inside the medium (i.e., fluorescence or phosphorescence)[5,6].

On the other hand, there are many practical issues that must be considered when collecting sets of data for use as input to an image reconstruction problem that do not affect the form of the equation to be solved or the formulas for $\mathbf{W}$, but that can significantly affect the quality of the result finally obtained (see Figure 1). One such issue is the choice of source

Figure 1

1A

1B

1C

1D

1E
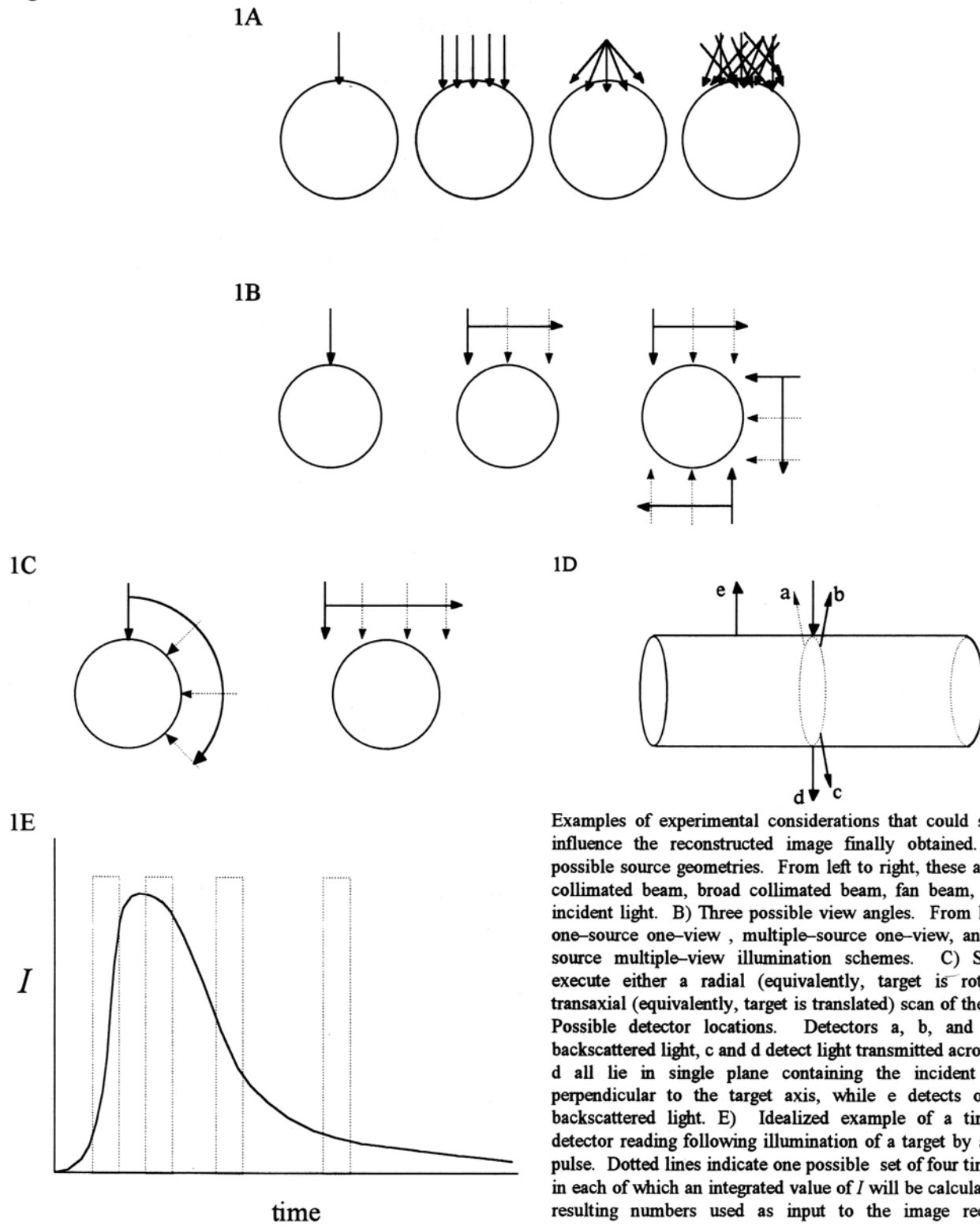
Examples of experimental considerations that could significantly influence the reconstructed image finally obtained. A) Four possible source geometries. From left to right, these are a narrow collimated beam, broad collimated beam, fan beam, and diffuse incident light. B) Three possible view angles. From left to right, one–source one–view , multiple–source one–view, and multiple–source multiple–view illumination schemes. C) Source may execute either a radial (equivalently, target is rotated) or a transaxial (equivalently, target is translated) scan of the target. D) Possible detector locations. Detectors a, b, and e measure backscattered light, c and d detect light transmitted across target; a–d all lie in single plane containing the incident beam and perpendicular to the target axis, while e detects out–of–plane backscattered light. E) Idealized example of a time–resolved detector reading following illumination of a target by a brief light pulse. Dotted lines indicate one possible set of four time windows in each of which an integrated value of I will be calculated, and the resulting numbers used as input to the image reconstruction algorithm. The number, locations and widths of the time windows are free parameters.

geometry: the incident light may be either collimated or diffuse, and can be produced in the form of narrow, broad, or fan beams. A second is the choice of *view angle*: is it sufficient to illuminate the target at a single point, or at multiple points but from a single direction, or is it necessary to illuminate at many different locations on the surface and from different directions? If a single view angle is not sufficient, one must decide whether it is preferable to perform radial or transaxial scans of the source about the target, or whether both types may be required. A third issue is the number and placement of detectors: for certain practical reasons[7,8], image reconstructions that employ only backscatter data (*i.e.*, detectors on the same surface and in the vicinity of the illuminated area) might be preferred, but it may be that readings from detectors farther from the source and/or in geometries closer to transmission are necessary in order to produce an accurate reconstruction. Another entire set of questions is associated with the choice of illumination scheme. There are many potential advantages to using time domain and frequency domain, rather than cw, methods[9,10], but at the cost of greater experimental effort and a larger body of data to be processed. If time domain data are collected, a decision must be made whether to work directly with the temporal profiles or with various calculated moments thereof. If the time domain data are processed directly, the number of data points taken from each one, their positions within the profile, and the widths of the associated time windows must be chosen. Similarly, if frequency domain data are collected, the specific modulation frequencies and the number of modulation frequencies employed must be chosen. When data corresponding to more than one source–detector separation, time window, and/or modulation frequency (ω) are available, they may all be processed simultaneously, or a more elaborate scheme may be adopted that considers only a subset of the data at first and then admits more in each subsequent stage[2,8,11].

Because the form of (1) does not in itself suggest a preference for any one answer to these questions over any other, all of these factors must be treated as "free parameters" for which those performing a measurement are free to choose whatever values they find most convenient. However, it is reasonable to suppose that the quality of the recovered image could be strongly dependent on the particular choices that are made. The issues of limited view angle and spatial distribution of detectors have been addressed to some extent in some of our other work[6,12,13]. In an effort to systematically extend these studies, we have used Monte Carlo simulations to acquire a large set of data that we can use to study the impact of different choices for all the free parameters on the quality of the reconstructed image. The ultimate goal of these studies is to identify at least one type of measurement that is optimal, in the sense of affording the best compromise among the different (and sometimes conflicting) goals of obtaining the most accurate image possible, reducing the physical effort involved in collecting the data, and reducing the computational effort involved in recovering the image. One particular concern in this work is the issue of the effect of errors in the elements of ΔI and/or $\mathbf{W}$ on the reconstructed image. Some of the sources of error were intentionally introduced in order to study their impact. As explained below, random error, or noise, was the most significant source of error in some cases, and systematic error, or bias, was the most significant in others. As shown below, each of these tends to produce a different characteristic type of error in the reconstructed image.

2. Methods

2.1 Collision Density Computations

The medium modeled was a cylinder (see Figure 2) with the following properties: uniform composition, isotropic scattering phase function, infinitely long axis, diameter = 20 mean free pathlengths (mfp), absorption cross section (Σ_a) = 0.0, scattering cross section (Σ_s) = total cross section (Σ_t) ≡ 1.0, refractive index ratio (internal/external) = 4/3. Three separate computations were performed. In each one, an ideal collimated point source launched 2×10^8 photons into the cylinder from one point on its surface; in each case incident beam lay in a plane perpendicular to the cylinder axis. The angles between the three incident beams and a normal to the surface were 0°, 22.02°, and 38.68°. Equivalently, the second and third positions (labeled b and c in Figure 2) were displaced from the first (labeled a in Figure 2) by a distance of 3.75 mfp and 6.25 mfp, respectively, in a direction orthogonal to both the incident light and the cylinder axis (see Figure 3C). Photons from sources b and c did not refract upon entering the medium, thus modeling an experiment in which light enters the target through an index–matching material.

The region in the vicinity of the source was sectioned into forty one layers, each one mfp in thickness. Every layer was further divided into four hundred voxels, each having a volume of $\pi/4$ mfp^3. As a photon propagated through the cylinder, the computation kept track of the total distance it had traveled; as the speed of light, c, is constant in a uniform

medium, this distance is proportional to its time of flight. A photon history was terminated when it either escaped from the medium or propagated a total distance of five hundred mfp.

Figure 2
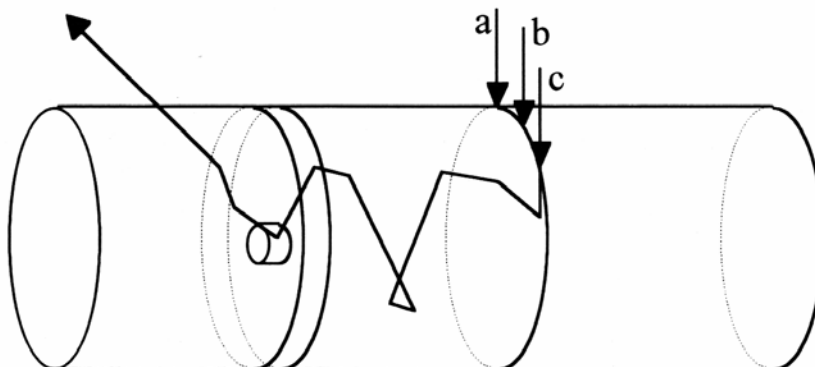
Medium modeled in collision density computations. Cylinder is homogeneous, isotropically scattering, with $\Sigma_a = 0.0$, $\Sigma_s = \Sigma_t = 1.0$. Axis is infinitely long, radius = ten mfp. Photons enter at one of positions a, b, and c, and propagate through medium until they escape or travel a total distance of 500 mfp in the interior. Internal reflection due to refractive index mismatch at the surface ($n_i/n_e = 4/3$) causes some increase in the mean duration of the photon histories; in the computations, the average number of internal reflections per incident photon was ~0.75. The volume lying within twenty mfp of the source along the cylinder axis was divided into forty one layers, each containing four hundred voxels. The volume of each voxel was $\pi/4$ (~0.79) mfp^3. Collisions were counted as a function of the voxel and the propagation distance (time) of the photon prior to the collision.

A one thousand–element array associated with each voxel counted the number of collisions (*i.e.*, scatterings) in the voxel as a function of the distance (time) the photon had propagated prior to the collision; the distance intervals corresponding to the array elements were 0.0–0.5, 0.5–1.0, 1.0–1.5, ..., 499.0–499.5, 499.5–500.0 mfp. Because of the medium and source geometries, it was possible to impose fourfold symmetry on the computed result in the case of source position a, and twofold symmetry in the other two cases. The total number of collisions recorded in each interval during the computation was subsequently normalized to the number of photon histories, voxel volume, and time interval to yield the per–photon collision density, ψ, at that location in the medium and time following an input pulse. This quantity is directly proportional to the light intensity, ϕ, at that location and time: $\phi = S\psi/\Sigma_t$, where S is the source strength.

Empirically, it was found that the decision to compute the collision densities in layers as much as twenty mfp away from the source along the cylinder axis was more than adequate to capture all photon collisions taking place within the allotted five hundred mfp propagation distance; in some of the results shown below, and in other work by our group[6,11], the weight function calculations used only data from layers up to ten mfp away from the source. Likewise, the decision to allow each photon to propagate up to five hundred mfp was excessively conservative; in practice far more than 99.9% of all incident photons escaped from the medium before they had traveled as much as three hundred mfp.

2.2 Detector Reading Computations

Detector readings were computed for the reference medium described above and for three target media. Each of these had the same dimensions and background properties as the reference, but contained in addition either one or thirteen black absorbers ($\Sigma_a = \infty$). These were infinitely long cylindrical rods of constant diameter, parallel to the cylinder axis (see Figure 3). The cross–sectional area of the rod in the one–absorber targets was π mfp^2, and so occupies 1% of the total volume of the cylinder. The cross–sectional area of each rod in the thirteen–absorber target was $\pi/16$ mfp^2; that is, the cumulative volume of the thirteen absorbers was a smaller percentage (.8125%) of the cylinder volume than the single rod in the other targets. However, distributed as they are in the target, they constitute a very strong violation of the weak perturbation premise underlying the validity of (1).

Figure 3
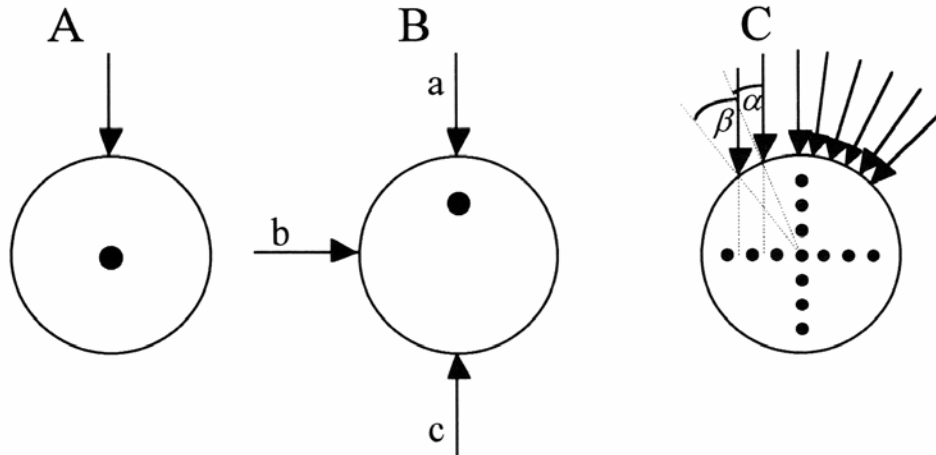
Absorber and source geometries for detector reading computations. In all cases, incident beam lies in the plane of the page, perpendicular to the cylinder axis. A) Absorber radius is one mfp; source beam is directed along a surface normal; because of the target symmetry, a source directed along any other surface normal would produce the same set of detector readings. B) Absorber radius is one mfp; all sources are directed along surface normals; because of the target symmetry, the detector readings that would be produced by a fourth source diametrically opposite b would be the mirror image of those obtained with source b. C) Thirteen rods in a cruciform array; radius of each absorber is 0.25 mfp; distance between centers of nearest neighbors is 2.5 mfp. Six normally directed sources are modeled at 9° intervals with respect to the arms of the absorber array; because of the target symmetry, these are the basis for a set of forty sources distributed at regular intervals about the target. Two non–normal sources are modeled at the indicated positions; as in the collision density computations, photons do not refract upon entering the target. The angles α and β are, respectively, 22.02° and 38.68°; the lateral displacement of these positions from the normal are, respectively, 3.75 and 6.25 mfp; because of the target symmetry, these are the basis for a set of four transaxial scans of the source across the target, with five source positions in each.

In the one–absorber computations, 5×10^7 photons were simulated, and there were no internal reflections at the boundary, thus modeling a target suspended in an index–matching fluid. As the weight functions were calculated from collision density data for a reference medium with an index–*mis*matched boundary, this is a source of systematic error in the image reconstructions for these media. In the thirteen–absorber computations, 2×10^8 photons were simulated, and the same index mismatch was present at the boundary as in the collision density computations. The detector reading computations for the reference and target media were not independent, but employed correlated sampling as a variance reduction technique[5,14]. Paired with every photon propagating in the reference is another following exactly the same trajectory in the target. Consequently, it is detected at the same place and time in both media unless its trajectory passes through an absorber inside the target. In this case, it contributes to a detector reading for the reference medium but not the target.

The target surface lying within twenty mfp of the source along the cylinder axis was divided into forty one bands, each with a width of one mfp. These were further divided into thirty six "rectangles," each with an area of $5\pi/9$ mfp^2 (see Figure 4). A five hundred–element array associated with each patch counted the number of photons exiting the cylinder within that area as a function of the distance (time) the photon had propagated prior to the collision, thus modeling the response of uncollimated cosine detectors; the distance intervals corresponding to the array elements were 0.0–1.0, 1.0–1.0, ..., 498.0–499.0, 499.0–500.0 mfp. Because of the medium and source geometries, it was always possible to impose at least twofold symmetry on the computed results, and fourfold symmetry in certain cases. The total number of exiting photon recorded in each interval during the computation was subsequently normalized to the number of photon histories, detector area, and time interval to yield the per–photon flux across the surface at that location and time following an input pulse. Although detector readings were computed for locations up to twenty mfp from the source along the cylinder axis, only detector readings in the band labeled 0 in Figure 4 were actually used as input in the image reconstructions presented below.

Figure 4
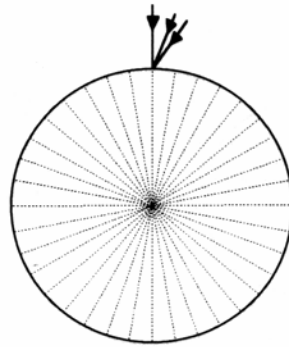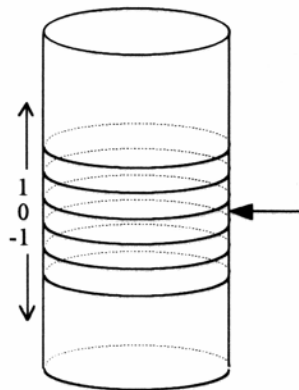
Distribution of detectors on target surface. The surface is first divided into bands, by the same planes that define the voxel layers in the interior. Each band is subdivided into thirty six parts, each subtending a central angle of 10°. As the cylinder radius is ten mfp, the surface area corresponding to each detector is $5\pi/9$ (~1.75) mfp². All photons exiting from the target are counted, corresponding to detecting emerging light with uncollimated cosine detectors. Non–normal source geometries were modeled by rotating the incident beam about the illuminated point and rotating the absorber array, if present, through the same angle.

Time–resolved (tr) detector readings for time windows of finite width were calculated by summing integrating the computed temporal profiles over all time points (*i.e.*, distance intervals) lying within the specified windows. The cw detector readings were calculated by integration of entire profiles. Detector responses in the frequency domain were obtained by calculating discrete Fourier transforms (FT) of the profiles. As no photons actually propagated more than five hundred mfp in the reference medium, there was no underestimate of cw detector response in the former calculation, nor any high–frequency artifacts in the latter that would be caused by truncation of the temporal profiles.

2.3 Weight Function Calculations

The weight function for a given source–detector configuration is a function of the temporospatial light intensity distribution in the interior of the reference medium, and of the *adjoint*, which is the set of detector responses resulting from a unit–strength source located at any point in the same medium. According to an established reciprocity theorem[15], the latter is equivalent to the interior light intensity distribution that results from launching photons into the medium from the detector. Therefore, each weight function was calculated from two sets of collision density data, after rotating one set in order to locate the source at the center of the area element corresponding to the detector. The collision density distribution for a normally–directed source was always used as the estimate of the adjoint. Therefore, the weight function calculated was actually the appropriate one for a measurement made with a collimated point source *and* a collimated point detector, while the computed detector readings were those for uncollimated cosine detectors covering a finite area. This mismatch between the detectors is a source of systematic error in the weight functions.

The formulas for calculation of weight functions are functions of the illumination scheme used and the optical property being imaged[5,6]. The weight for a cw measurement is proportional to the product of the intensity and adjoint. The weight for a frequency domain measurement is proportional to the product, at the frequency of interest, of the FTs of the tr intensity and adjoint; in contrast to the cw case, this is a product of complex numbers. The weight for a time domain measurement is proportional to the convolution of a tr intensity and adjoint; alternatively, it may be calculated from the inverse FT of a set of frequency domain weights, if the latter are known at many modulation frequencies. Because the targets contain black–body absorbers, only the absorption weight functions need to be calculated for the image reconstructions presented here. The relevant formulas are

$$w_{ijk} = \frac{-1}{4\pi}\left(\phi_{ij}\phi_{ik}^+ - 3\mathbf{J}_{ij}\cdot\mathbf{J}_{ik}^+\right),$$

$$w_{ijk}(t) = \frac{-1}{4\pi}\left[\phi_{ij}(t)\otimes\phi_{ik}^+(t) - 3\mathbf{J}_{ij}(t)\otimes\mathbf{J}_{ik}^+(t)\right], \quad (2)$$

$$w_{ijk}(\omega) = \frac{-1}{4\pi}\left[\overline{\phi}_{ij}(\omega)\overline{\phi}_{ik}^+(\omega) - 3\overline{\mathbf{J}}_{ij}(\omega)\cdot\overline{\mathbf{J}}_{ik}^+(\omega)\right],$$

for the cw, time domain, and frequency domain cases, respectively. In these equations, the subscripts i, j, and k denote voxel, source, and detector, respectively, the superscript + denotes the adjoint, a bar above a quantity denotes the FT, and $\otimes$ denotes the operation of convolution:

$$f(t) \otimes g(t) \equiv \int_0^t f(\tau)g(t - \tau)d\tau,$$

$$\mathbf{f}(t) \otimes \mathbf{g}(t) \equiv \int_0^t \mathbf{f}(\tau) \cdot \mathbf{g}(t - \tau)d\tau.$$

In practice, the second term in (2) was neglected, as it is expected for two reasons to be a small correction. First, with the possible exception of voxels in the immediate vicinity of the source (detector), $|\mathbf{J}| \ll \phi$ ($|\mathbf{J}^+| \ll \phi^+$). Second, angles close to 90° between $\mathbf{J}$ and $\mathbf{J}^+$ may be typical.

2.4 Image Reconstruction Algorithms

For the study on the dependence of frequency domain image quality on ω, the conjugate gradient descent (CGD) algorithm[1,2,6] was employed for the reconstructions. The vector, ΔI, of absolute differences in detector readings between the target and reference media is analyzed by this algorithm, which arrives at a final estimate of $\Delta \mathbf{x}$ by repeatedly applying the formula

$$\Delta \mathbf{x}^n = \Delta \mathbf{x}^{n-1} - \alpha^n \mathbf{d}^n,$$

where

$$\alpha^n = \frac{\left(\mathbf{g}^{n-1}\right)^{\mathrm{T}} \mathbf{g}^{n-1}}{\left(\mathbf{d}^n\right)^{\mathrm{T}} \mathbf{A} \mathbf{d}^n}, \qquad \mathbf{d}^n = -\mathbf{g}^{n-1} + \beta^n \mathbf{d}^{n-1},$$

and

$$\beta^n = \frac{\left\|\mathbf{g}^{n-1}\right\|^2}{\left\|\mathbf{g}^{n-2}\right\|^2}, \qquad \mathbf{g}^n = \mathbf{A}\Delta\mathbf{x}^n - \mathbf{b} = \mathbf{g}^{n-1} - \alpha^n \mathbf{A} \mathbf{d}^n,$$

$$\mathbf{A} \equiv \mathbf{W}^{\mathrm{T}} \mathbf{W}, \qquad \mathbf{b} \equiv \mathbf{W}^{\mathrm{T}} \Delta I.$$

At the outset, an initial guess, $\Delta \mathbf{x}^0$, must be taken for the unknown, and the initial values for the other quantities are $\beta^1 = 0$, $\mathbf{g}^0 = \mathbf{A}\Delta\mathbf{x}^0 - \mathbf{b}$, $\mathbf{d}^1 = -\mathbf{g}^0$. For the results presented here, the dimension of $\Delta\mathbf{x}$ was reduced by summing the weights in voxels at equivalent locations in different layers. That is, prior knowledge of the translational invariance of the target along the cylinder axis was assumed.

The other results presented here were obtained with the SART–type algorithm previously described[3,5,7,8]. The data used as input to this algorithm are the *relative* differences in detector reading, $\Delta I/I_0$, between the target and reference media, where I_0 denotes the reference medium detector reading. The estimate of the unknown, Δy (a different symbol is used here because the calculated quantity is *not* an estimate of the absolute perturbation, $\Delta\mathbf{x}$ in an optical cross section) is repeatedly modified according to the formula

$$\Delta y_i^{n+1} = \Delta y_i^n + \frac{\sum_{j,k} w_{ijk}\left[\left(\frac{\Delta I_{jk}}{I_{0,jk}}\right) - \frac{\sum_i w_{ijk}\Delta y_i^n}{\sum_i w_{ijk}}\right]}{\sum_{j,k} w_{ijk}}.$$

For the results presented here, no summing of weights in different layers was performed; a seperate update was computed for every voxel in every iteration. However, after each iteration of the algorithm was complete, the individual–voxel values of Δy_i^n were replaced by the corresponding averages calculated over all layers.

There is an advantage to using an algorithm that analyzes relative detector reading differences, in that some practical difficulties associated with accurate measurement of absolute changes are circumvented. These include variability in the light source output over an extended time scale and the need for periodic absolute quantitation of detector efficiencies. An unfavorable feature, at least of this particular algorithm, is that the relation between Δy and Δx is not known. There are clear indications of a positive but nonlinear correlation between them; until the relationship is identified, images produced by the SART-type algorithm can't be used as the basis for revising the computations of collision densities.

For all results presented below, a positivity constraint was imposed on the computed image intensity in every voxel after every iteration. Aside from this and those already described, no constraints or regularization techniques were employed.

3. Results

3.1 Detector readings and collision densities

Some representative examples of $\Delta I/I_0$ vs. detector location, for the thirteen–absorber target, are shown in Figure 5. Each panel contains data for two different normally–directed source locations. Note that in the case of a cw measurement, $\Delta I/I_0$ is

Figure 5
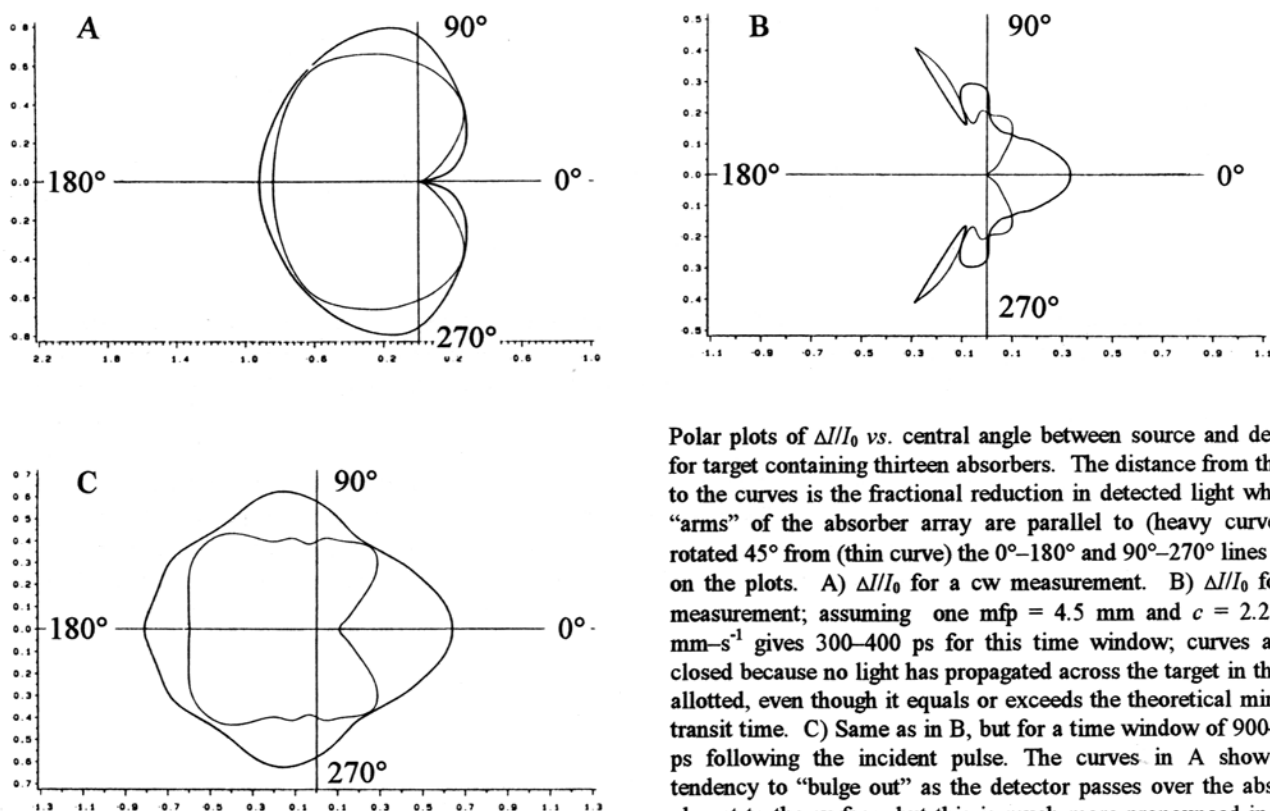
Polar plots of $\Delta I/I_0$ vs. central angle between source and detector, for target containing thirteen absorbers. The distance from the pole to the curves is the fractional reduction in detected light when the "arms" of the absorber array are parallel to (heavy curve) and rotated 45° from (thin curve) the 0°–180° and 90°–270° lines drawn on the plots. A) $\Delta I/I_0$ for a cw measurement. B) $\Delta I/I_0$ for a tr measurement; assuming one mfp = 4.5 mm and $c = 2.25 \times 10^{11}$ mm-s^{-1} gives 300–400 ps for this time window; curves are not closed because no light has propagated across the target in the time allotted, even though it equals or exceeds the theoretical minimum transit time. C) Same as in B, but for a time window of 900–1,000 ps following the incident pulse. The curves in A show some tendency to "bulge out" as the detector passes over the absorbers closest to the surface, but this is much more pronounced in B and C.

very small at angles near backscattering, although the most superficial absorber is only 2.25–2.75 mfp from the surface. In contrast, as a narrow time window progresses from very early to later portions of the tr readings, the detectors receive light that has propagated farther, and thus deeper, and detect an appreciable difference between the target and reference. If it is assumed that the mfp is 4.5 mm and c is 2.25×10^{11} mm–s^{-1}, as was the case in experiments recently performed by Das *et al.*[16], then the time windows corresponding to the data in Panels B and C of Figure 5 are, respectively, 300–400 ps and 900–1,000 ps subsequent to the incident pulse. The corresponding data for the one–absorber targets (**not shown**) show, as expected, that $\Delta I/I_0$ is much smaller for these media.

Examples of processed data obtained from the collision density computations are shown as **contour plots** in Figure 6. The specific data presented are for the layer of voxels containing the incident beam, and are the **output at specific frequencies** of the discrete FTs of the tr collision densities. In the real part of the specific case shown in the Figure, there is one curve along which a transition from positive to negative values occurs, while the imaginary part has the same sign in all voxels; the spatial frequency increases with increasing ω, resulting in a larger number of sign changes.

Figure 6
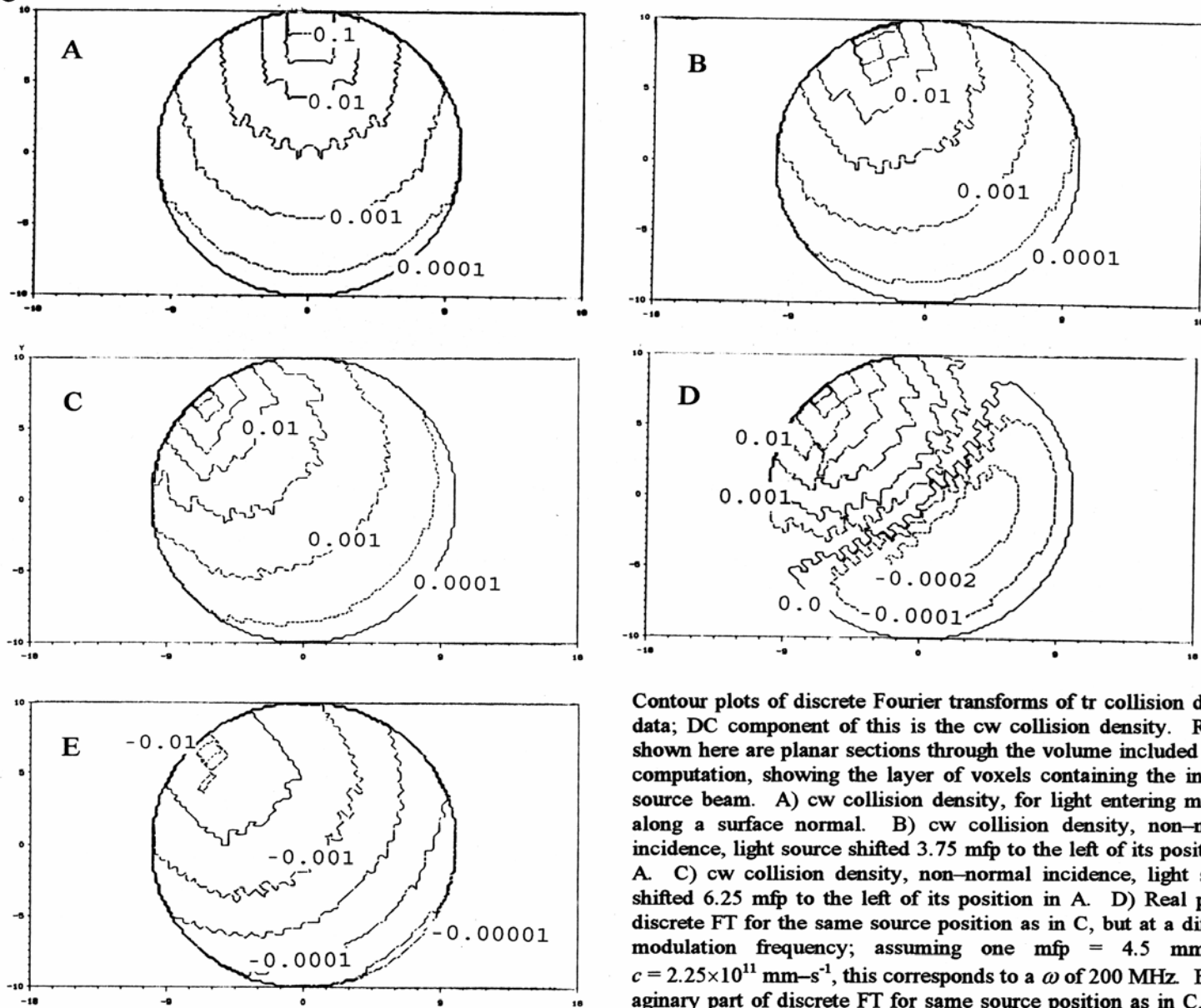
Contour plots of discrete Fourier transforms of tr collision density data; DC component of this is the cw collision density. Results shown here are planar sections through the volume included in the computation, showing the layer of voxels containing the incident source beam. A) cw collision density, for light entering medium along a surface normal. B) cw collision density, non–normal incidence, light source shifted 3.75 mfp to the left of its position in A. C) cw collision density, non–normal incidence, light source shifted 6.25 mfp to the left of its position in A. D) Real part of discrete FT for the same source position as in C, but at a different modulation frequency; assuming one mfp = 4.5 mm and $c = 2.25\times10^{11}$ mm–s^{-1}, this corresponds to a ω of 200 MHz. E) Im–aginary part of discrete FT for same source position as in C, same ω as in D.

3.2 One absorber, on cylinder axis

Images reconstructed, using the SART-type algorithm, of the one–absorber target in which the absorber was on the cylinder axis (see Figure 3A) are shown in Figure 7. The cw reconstruction (Panel A) used detector readings for a single source location and assumed prior knowledge of the radial symmetry of the target. The tr reconstruction (Panel B) used four source locations at 90° intervals about the target and identical set of detector readings, with respect to the source, were obtained at all four. All detector readings were processed simultaneously in the cw reconstruction. The tr reconstruction used a previously described progressive algorithm[11], in which data from the earliest time window only is processed at first and at each subsequent step an additional time window is included; data from ten time windows were ultimately used. These correspond to light that has propagated a total distance of 0–5, 5–10, ..., 45–50 mfp in the medium. Using the same assumptions as before, these are equivalent to 0–100 ps, 100–200 ps, ..., 900 ps – 1 ns following the incident pulse. Inspection of the cw image reveals that while it contains no artifacts, the width of the peak is greater than that of the target and its edge detection is imperfect. The correct peak width and edge resolution are seen in the tr image, although the height of the peak is not uniform; the image intensity in the central voxel is ~80% of that in the second ring of voxels.
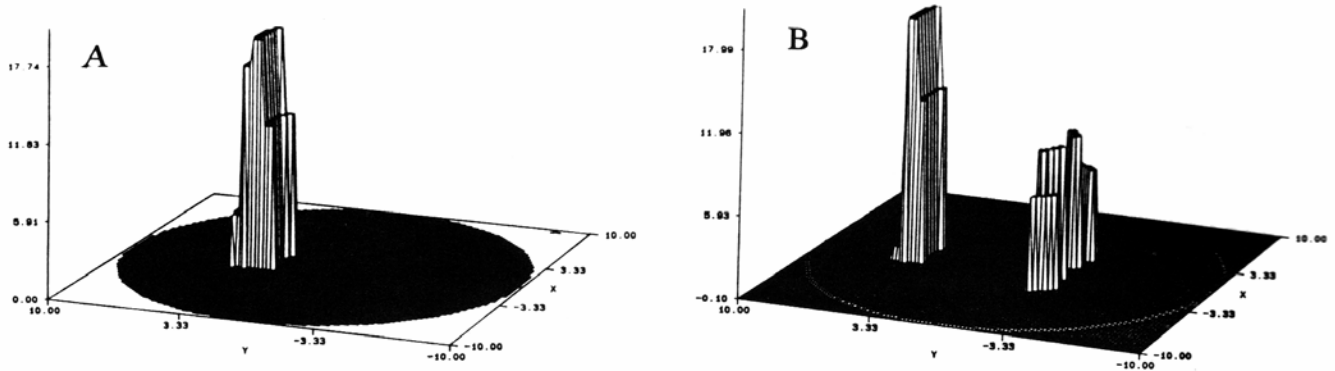
Figure 7
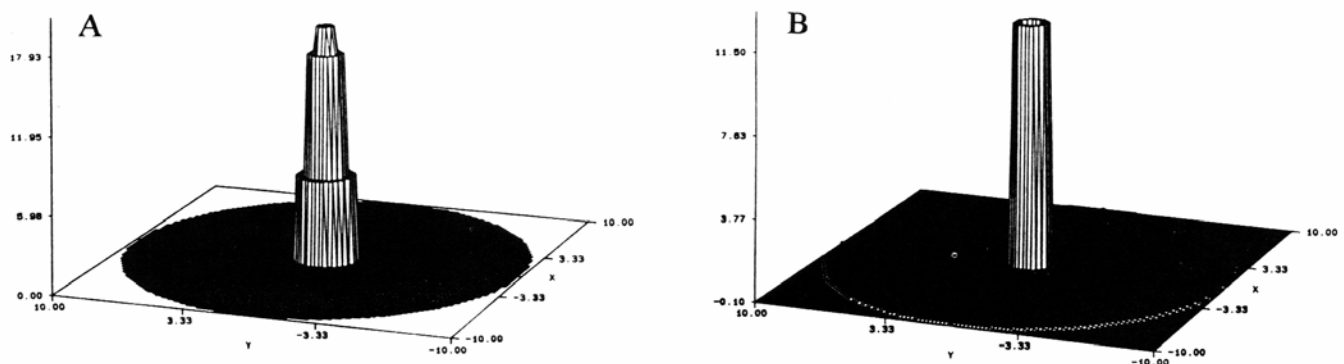
Surface plots of reconstructed images of one–absorber target with rod on cylinder axis, using SART-type algorithm. A) Image derived from cw data; all (thirty six) detector readings were processed at once, and prior knowledge of target's radial symmetry was assumed; 10,000 iterations of the algorithm were computed. B) Image derived from tr data. Detector readings corresponding to ten time windows were used; if it is assumed that one mfp = 4.5 mm and $c = 2.25 \times 10^{11}$ mm–s^{-1}, the time windows are 0–100 ps, 100–200 ps, ..., 900 ps – 1 ns after the incident pulse. Only data from the first time window were considered initially, and one hundred iterations of the algorithm computed, data from the second time window were then added, and another two hundred iterations computed, *etc.* After the detector readings from all ten time windows were incorporated, an additional 10,000 iterations were computed.

3.3 One absorber, off cylinder axis

Images reconstructed, using the SART-type algorithm, of the one–absorber target in which the absorber was not on the cylinder axis (see Figure 3B) are shown in Figure 8. Both the cw (Panel A) and tr reconstruction (Panel B) used four source locations at 90° intervals about the target (see legend to Figure 3). As in the preceding case, all detector readings were processed simultaneously in the cw reconstruction and a progressive algorithm was used for the tr reconstruction. The same time windows were used in the latter case as in the reconstruction of the target containing an on–axis rod. Inspection of the cw image reveals that while it contains no artifacts, there is a significant systematic error, with the peak lying closer to the center in the image than it does in the target. The correct peak location is seen in the tr image, but four voxels contain an artifact whose maximum image intensity is ~53% of that in the image peak. An attempt was made to compensate for the varying degrees of uncertainty in the computed $\Delta I/I_0$s (see Discussion) by assigning a confidence factor in the range 0.0–1.0 to each relative difference value, and the tr reconstruction was repeated. The maximum height of the artifact peaks in the new result (not shown) was reduced ~12% relative to that in Panel B.

Figure 8

A

B

Surface plots of reconstructed images of one–absorber target with rod halfway between cylinder axis and surface, using SART-type algorithm. A) Image derived from cw data; all (thirty six) detector readings were processed at once; 10,000 iterations of the algorithm were computed. B) Image derived from tr data. The same time windows and data analysis sequence were used here as for the result in Figure 7B.

Images reconstructed of the same target, using the CGD algorithm and frequency–domain detector readings (*i.e.*, FTs of computed absolute ΔIs) and weights are shown, as a function of ω, in Figure 9. As for the cw and tr results, these reconstructions incorporated data for four source locations at 90° intervals about the target, and thirty six detectors per source. A single frequency was used for each of these reconstructions. In contrast to the preceding cases, the physical length assumed for one mfp was 1.125 mm. Inspection of the results reveals that no significant change from the cw result is seen until ω is at least 100 MHz. As in the case of the cw image produced by the SART-type algorithm, the peak lies too close to the center of the image when ω is $\leq$ 100 MHz. When ω = 1 GHz, the image quality is excellent, in terms of the location and size of the peak. At frequencies $\geq$ 10 GHz, the image bears no resemblance to the target; above 10 GHz, the FTs of the computed tr collision densities are dominated by noise.

3.4 Thirteen absorbers

A representation of an ideal reconstructed image of the thirteen–absorber target, and both cw and single time window images produced by the SART–type algorithm are shown in Figure 10. Although the thirteen absorbers all have the same diameter and Σ_a, when overlaid on the voxel grid the central absorber lies within a single voxel and all others fall on the boundary of either two or four voxels. Consequently, the peaks in the ideal image (Panel A) would have three different heights and four shapes. In addition, the spatial extent of the absorbers must always be overestimated, as the absorber diameter is less than the voxel dimensions. As some portions of the image invariably obstruct others in the surface plots, the reconstructed images are presented in the form of both surfaces and contour plots.

The images in Figure 10 were obtained using only detector readings for normally–directed sources (see Figure 3C). By means of rotations and/or reflections, the six distinct sets of computed detector readings was expanded into a set of forty source positions about the target; however, the reconstruction algorithm did not *impose* any symmetry planes on the image. The cw result (Panels B, C) suggests a perturbation distributed through the medium and in several unconnected parts, but with poor resolution of separate rods. It appears that either five or nine of the individual absorbers coalesce into a single central mass, with the remaining ones giving rise to a single image peak on each "arm" of the array. The one–time–window (*i.e.*, as in the cw case, all detector readings considered simultaneously) result (Panels D, E) used those data corresponding to 500–600 ps after the incident pulse (using an assumed value of 4.5 mm for one mfp) exhibits much better resolution. However, two of the three absorbers lying along each arm appear to coalesce into a single mass, and the most superficial absorbers are incorrectly located at the surface.

Having thus established that the information content needed for an accurate resolution of the absorber array into its
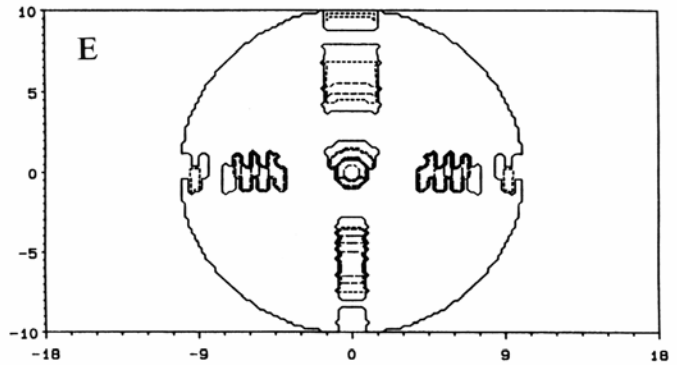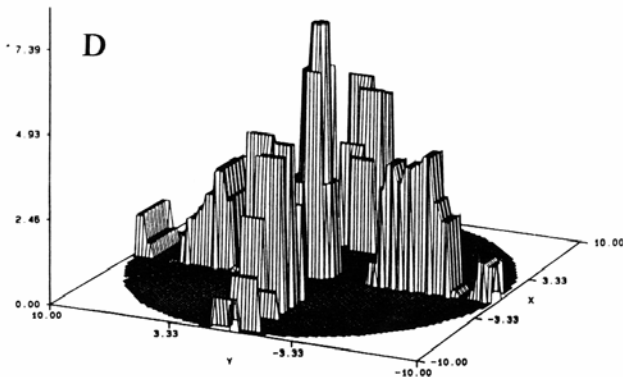
Figure 9

100 MHz   1 MHz   1 KHz   DC

1 THz   100 GHz   10 GHz   1 GHz
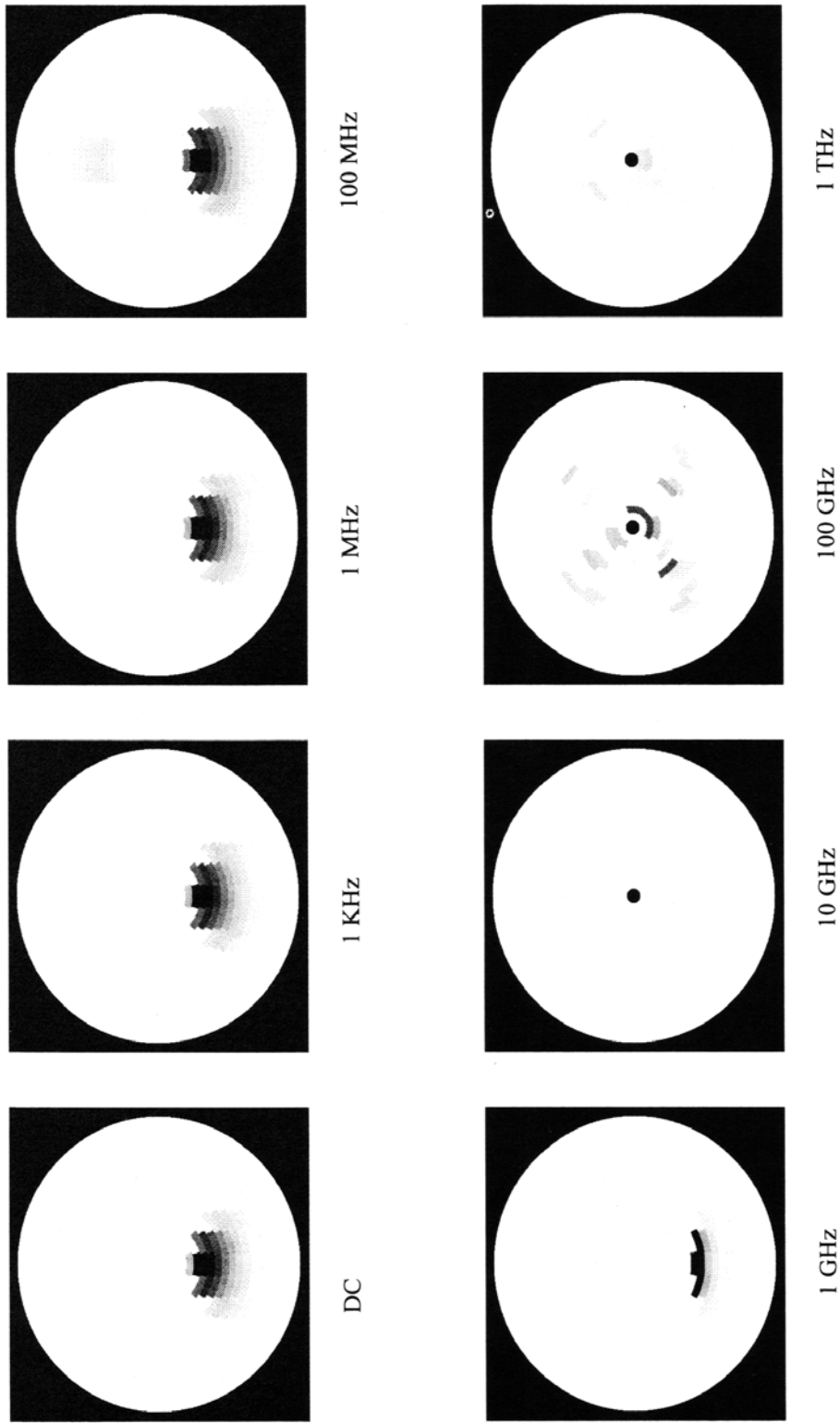
Single—frequency reconstructions of one—absorber target, obtained by CGD algorithm and FTs of computed absolute ΔIs. Results shown here are images after 100,000 iterations of the algorithm. Prior knowledge of the translational invariance of the target along the cylinder axis was assumed; weights in equivalent locations in all layers were summed. Peak location is correct in the 1 GHz image, and skewed toward the center at lower modulation frequencies. At modulation frequencies > 10 GHz, noise dominates the FTs of the time—resolved collision densities.

Figure 10

A

B

D
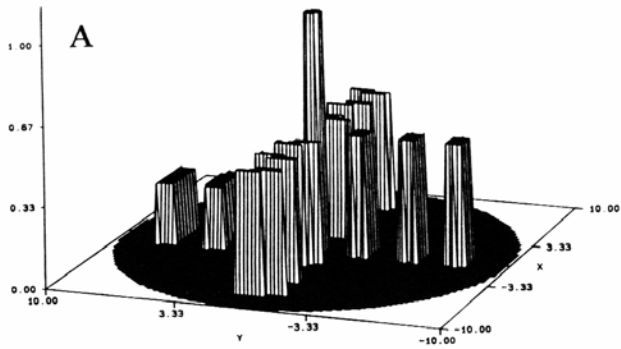
A) Ideal image reconstruction would contain thirteen fully resolved peaks, but their height and shapes would be distorted due to the shapes and large size, relative to the absorber diameters, of the voxels. B) Surface plot of cw image obtained by SART–type algorithm from forty normally directed sources, with thirty six detectors per source. C) Same result as in B, but displayed as a contour plot. D) Surface plot of a time resolved image obtained by SART–type algorithm from forty normally directed sources, with thirty six detectors per source, and detector readings for a single time window, 500–600 ps after the incident pulse (one mfp = 4.5 mm, $c = 2.25 \times 10^{11}$ mm–s^{-1}). E) Same result as in D, but displayed as a contour plot.

C

E
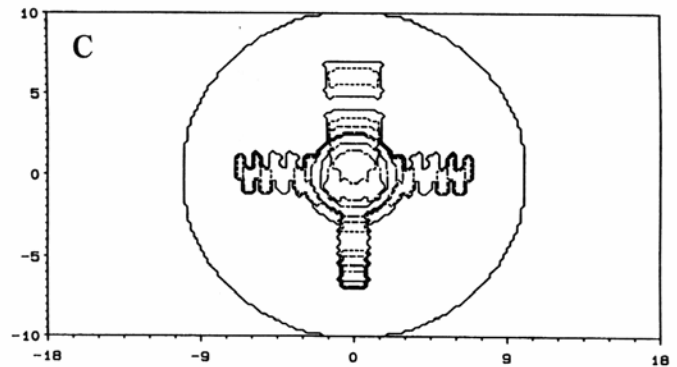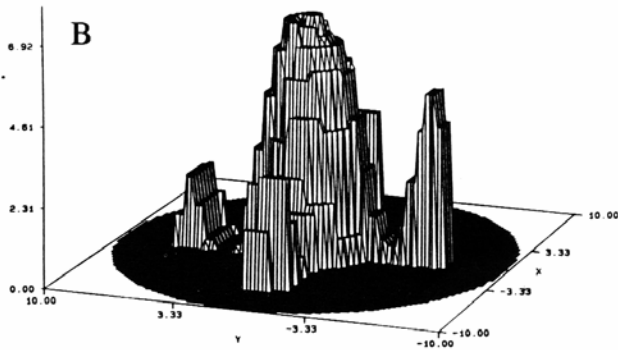
separate components is contained in the detector readings, additional images of this target were reconstructed using several different varieties of the SART–type algorithm. Some of the results obtained from these are shown in Figure 11.

In an attempt to address to incorrect location of the most superficial absorber seen in Figure 10D and 10E, detector readings corresponding to two time windows, 0–100 ps and 500–600 ps, were simultaneously processed to produce the image shown in Panels A and B. Only detector readings for normally directed sources were used in this reconstruction. In this result, there is resolution along the arms comparable to that seen in the one time window image, and the location of the most superficial absorbers is accurate, but there is no peak at the center of the image, and it appears that the peaks corresponding to the central absorber's four nearest neighbors are coalesced into a ring surrounding the image's central void. The image intensity in this ring is reduced relative to those of more superficial peaks.

Three different tr images employing data for all ten previously specified time windows and the progressive algorithm, were then reconstructed. Panels C and D show the result obtained using only data for normally–directed sources, corresponding to a radial scan of the target by the source (forty source locations altogether; see Figure 1C). Panels E and F show the result obtained using only data for a combination of normally–directed and oblique sources that correspond to a set
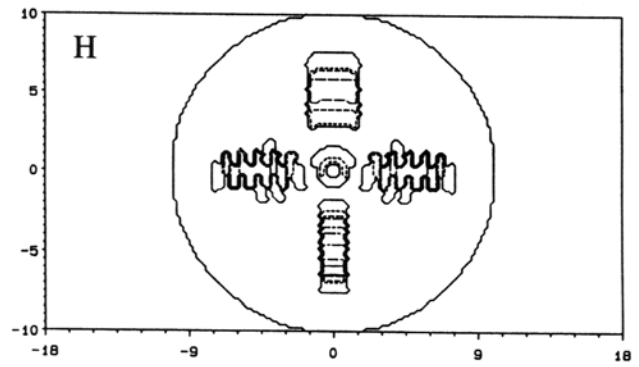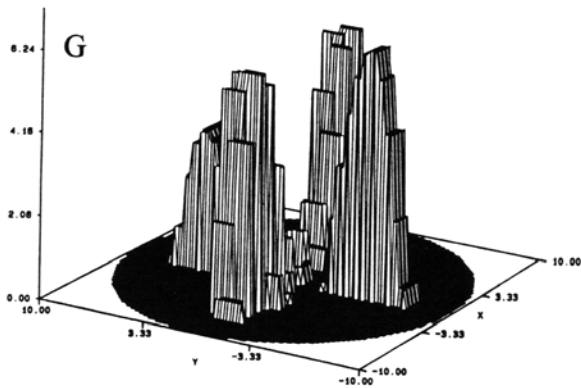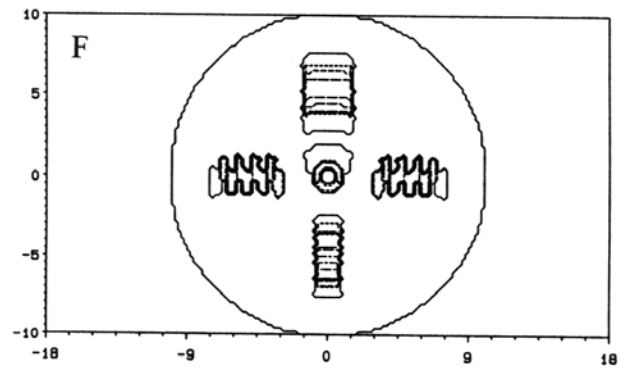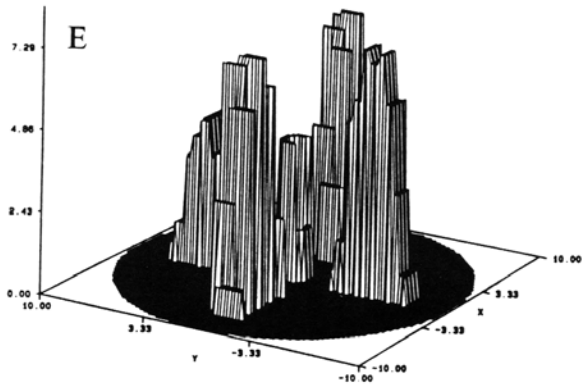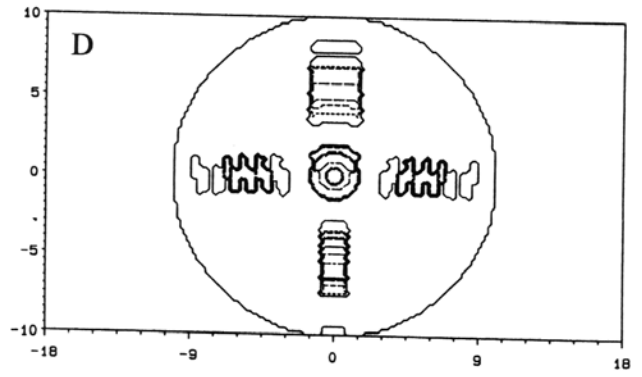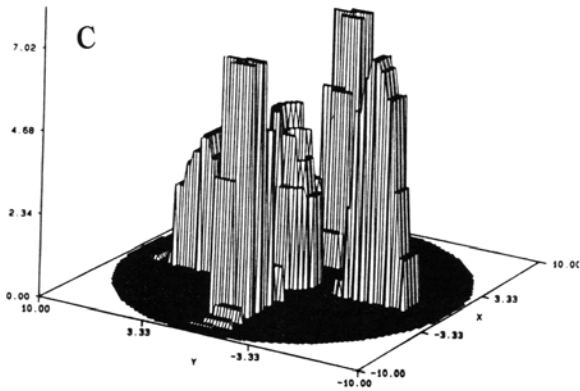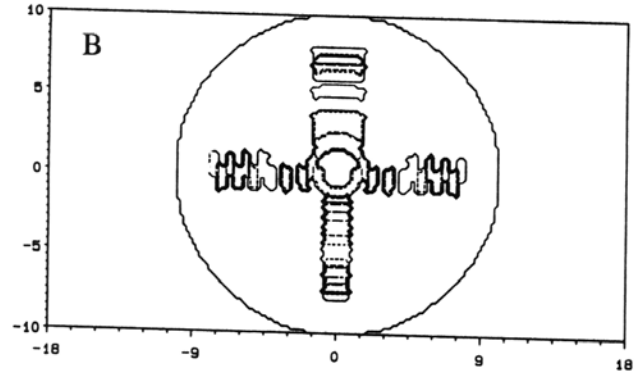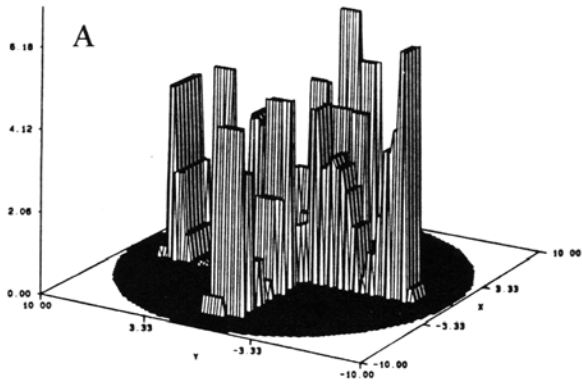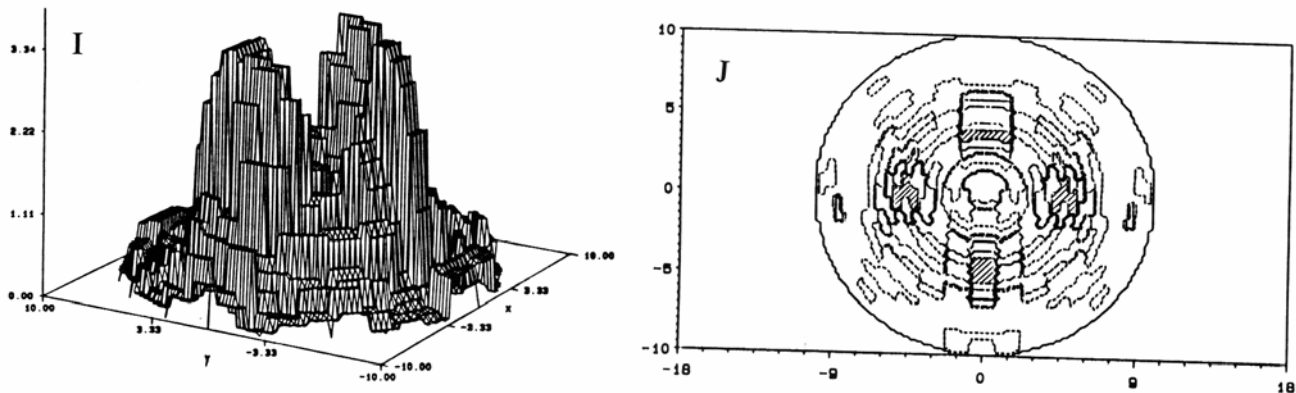
Surface and contour plots of time domain and frequency domain reconstructions of thirteen absorber target. SART–type algorithm was used in all cases. A,B) Image obtained using data for two time windows (0–100 ps and 500–600 ps), forty sources executing a radial scan of the target, thirty six detectors per source, and simultaneous (*i.e.*, non–progressive) processing of all detector readings. C,D) Image obtained using data for ten time windows (0–100 ps, ... 900 ps – 1 ns), forty sources executing a radial scan of the target, thirty six detectors per source, and progressive processing of detector readings. E,F) Image obtained using data for ten time windows (0–100 ps, ... 900 ps – 1 ns), twenty sources executing four transaxial scans of the target, thirty six detectors per source, and progressive processing of detector readings. G,H) Image obtained using data for ten time windows (0–100 ps, ... 900 ps – 1 ns), fifty six sources executing both radial and transaxial scans of the target, thirty six detectors per source, and progressive processing of detector readings. I,J) Image obtained using data for a single modulation frequency (200 MHz), forty sources executing a radial scan of the target, and thirty six detectors per source. Hatched areas (J) along each arm of the absorber array are the regions of greatest image intensity (> 6); central region image intensity is between 3 and 4.

of four transaxial scans of the target by the source, with the target rotated 90° between scans (twenty source locations altogether; see Figure 1C). Panels G and H show the result obtained using only data for all sources, corresponding to a combination of both radial and transaxial scans (fifty six source locations altogether). In every case, the image contains only five distinct peaks. It appears that at least two absorbers are coalesced into a single mass along each arm. In all three images, the image intensity of the central mass is reduced relative to the more superficial peaks, possesses a void at the center (in the first of the three images, the image intensity in the central voxel is positive but an order of magnitude smaller those in the adjacent rings; in the other two, it is exactly zero in the center), and is skewed in the +Y direction in the plots.

The frequency domain weights and detector readings for a single modulation frequency (ω = 200 MHz, assuming one mfp = 4.5 mm, $c = 2.25 \times 10^{11}$ mm–s^{-1}), and corresponding to a radial scan of the source about the target, produced the reconstruction shown in Panels I and J. This image contains considerably more artifact than any of the cw or tr reconstructions, but has the same five–peak qualitative structure as most of the others. There is a "saddle" structure in the central region; the image intensity there is a minimum with respect to that along the arms, but a maximum with respect to that along the diagonals.

4. Discussion

The purpose of this study was to examine the effects of certain factors related to physical measurement and computational complexity on the quality of images algebraically reconstructed from tomographic measurements of highly scattering media.

Examination of the tr detector reading data indicates that the impact of the absorbers on light reaching the detector increases monotonically with increasing time. The same qualitative behavior is to be expected for the light intensity distribution in the interior; therefore, the systematic error in tr weight functions calculated from the reference medium data increases with increasing time. The relative magnitudes of the errors in different weight functions is expected to be: early tr < cw ≈ frequency domain < late tr.

The images of the one–absorber targets demonstrate the different types of impact to be expected from systematic error (bias) in the computed weight functions and random error (noise) in both the weight functions and detector readings. In

the on–axis absorber case, the edge resolution was sharper in the tr than in the cw reconstruction, which suggests the principal effect of bias is to produce distortions in the image. The results from the off–axis absorber case corroborate this, as the distance from the axis to the peak is underestimated in the cw image but not in the tr image. The latter also contains a significant artifact. As the tr collision densities and detector readings were computed in Monte Carlo simulations, there is noise in the temporal profiles. The residual noise in the calculated cw collision densities and detector readings is very small because the domain of integration is the entire temporal profile. On the other hand, much smaller domains are used to calculate to the tr quantities, which are, consequently noisier. This suggests that the artifacts are a consequence of noise in the calculated weights and $\Delta I/I_0$s. This interpretation is strengthened by the observation that some reduction in the image intensity in the artifact peaks resulted when each $\Delta I/I_0$ (but *not* the weights) was modified with a "confidence factor." (This factor, η, monotonically from 0.0 to 1.0 as the number of detected photons corresponding to I_0 increases, and has the property that quadrupling the number detected produces a halving of $1 - \eta$.)

These conclusions regarding the effects of bias and noise are also corroborated by the single–frequency images of the off–axis one–absorber target. At low values for ω, for which the bias in the weight functions is expected to be comparable to that in the cw case, the distance from the axis to the absorber is underestimated and the spatial extent of the absorber is overestimated. As ω increases, the noise in the calculated weights and detector responses steadily increases, leading ultimately to cases in which the "image" contains nothing but artifacts. The single–frequency images of the off–axis one–absorber target also point to the conclusion that there may be some one modulation frequency that is optimal for probing a target at a specific depth. The 1 GHz image is comparable to the tr image in that the location and spatial extent of the absorber are correct, and the artifacts in former are significantly less prominent.

A requirement of a measurement–reconstruction protocol is successful resolution of multiple perturbations. We have previously accomplished this for media containing two absorbers whose $\Delta \Sigma_a$ is finite[1,4,16]. The thirteen–absorber target considered in this study contained infinitely long, closely juxtaposed, black absorbers. The principal conclusion to be drawn from the results is that a one–step perturbation method can not produce highly accurate images of a medium that violates the premises underlying (1) this strongly. The image obtained using data from a single, early time window is good in many respects, but attempts to improve it by using data from two or from ten time windows resulted in appreciably less accurate images. Many specific features are attributable to bias in the reference medium weight functions when applied to this target. This effect should be especially great near the axis, where the central absorber is shielded by four nearest neighbors; this results in a large overestimate of the weight, and a large underestimate of the image intensity. In order to do much better than the images shown here, it will be necessary to incorporate some type of correction for the interactions among different absorbers[17] into the reconstruction algorithm.

The quality of the image obtained when only data corresponding to transaxial scans of the source across the target is about the same as in that obtained when only data from radial scans was used, although the former set contains only half as many detector readings as the latter. Neither was there any improvement when both data sets were combined. It is probable that the effect of the previously described errors in the weight functions is to prevent an image of greater accuracy from being reconstructed in any event, although the issue of redundant detector readings must also be explored.

There are two significant features of the 200 MHz frequency domain image, relative to the cw image of the same target. One is the presence of appreciable artifacts in the former; these may be attributable to the greater degree of noise in the frequency domain weights and detector readings, and this may be confirmed in future studies employing higher ωs. The second is that, relative to the cw case, the image intensity is reduced in the central region and enhanced along the arms in the 200 MHz image. It was realized, in retrospect, that a single–frequency reconstruction, using the particular type of algorithm employed here, should not be expected to be better overall than the cw result. An algorithm employing data for multiple values of ω could, however, yield an improved reconstruction.

5. Acknowledgment

6. References

[1] Y. Wang, J. Chang, R. Aronson, R. L. Barbour, H. L. Graber, J. Lubowsky, "Imaging of scattering media by diffusion tomography: an iterative perturbation approach," *Proc. Physiological Monitoring and Early Detection Diagnostic Methods*, SPIE vol. 1641, pp. 58–71, 1992.

[2] J. Chang, Y. Wang, R. Aronson, H. L. Graber, R. L. Barbour, "Layer–stripping approach for recovery of scattering media from time–resolved data," *Proc. Inverse Problems in Scattering and Imaging*, SPIE vol. 1767, pp. 384–395, 1992.

[3] H. L. Graber, J. Chang, J. Lubowsky, R. Aronson, R. L. Barbour, "Near–infrared absorption imaging of dense scattering media by steady–state diffusion tomography," *Proc. Photon Migration and Imaging in Random Media and Tissues*, SPIE vol. 1888, pp. 372–386, 1993.

[4] W. Zhu, Y. Wang, H. L. Graber, R. L. Barbour, J. Chang, "A regularized progressive expansion algorithm for recovery of scattering media form time–resolved data," *Advances in Optical Imaging and Photon Migration*, Optical Society of America, vol. 21, pp. 211–216, 1994.

[5] H. L. Graber, J. Chang, R. Aronson, R. L. Barbour, "A perturbation model for imaging in dense scattering media: derivation and evaluation of imaging operators," *Medical Optical Tomography: Functional Imaging an Monitoring*, SPIE Institutes vol. IS11, pp. 121–143, 1993.

[6] J. Chang, H. L. Graber, R. L. Barbour, "Imaging diffusive media using time–independent and time–harmonic sources: dependence of image quality on imaging algorithms, target volume, weight matrix, and view angles," accompanying paper in these proceedings.

[7] R. L. Barbour, H. L. Graber, R. Aronson, J. Lubowsky, "Imaging of subsurface regions of random media by remote sensing," *Proc. Time–Resolved Spectroscopy and Imaging of Tissues*, SPIE vol. 1431, pp. 192–203, 1991.

[8] R. L. Barbour, H. L. Graber, J. Lubowsky, R. Aronson, B. B. Das, K. M. Yoo, R. R. Alfano, "Imaging of diffusing media by a progressive iterative backprojection method using time–domain data," *Proc. Physiological Monitoring and Early Detection Diagnostic Methods*, SPIE vol. 1641, pp. 21–34, 1992.

[9] K. M. Yoo, B. B. Das, F. Liu, R. R. Alfano, "Ultrashort laser pulse propagation and imaging in biological tissue and model random media – steps towards optical tomography," *Medical Optical Tomography: Functional Imaging an Monitoring*, SPIE Institutes vol. IS11, pp. 425–449, 1993.

[10] E. M. Sevick, C. L. Burch, J. K. Frisoli, M. L. Johnson, K. Nowaczyk, H. Szmacinski, J. R. Lakowicz, "The physical basis of biomedical optical imaging using time–dependent measurements of photon migration in the frequency–domain," *Medical Optical Tomography: Functional Imaging an Monitoring*, SPIE Institutes vol. IS11, pp. 485–512, 1993.

[11] J. Chang, Y. Wang, R. Aronson, H. L. Graber, R. L. Barbour, B. Das, J. Dolne, K. M. Yoo, R. R. Alfano, "Time–resolved imaging in dense scattering media," *Proc. Physiological Imaging, Spectroscopy, and Early–Detection Diagnostic Methods*, SPIE vol. 1887, pp. 108–119, 1993.

[12] J. Chang, H. L. Graber, R. L. Barbour, "Progress toward optical mammography: imaging in dense scattering media using time–independent optical sources," *Proc. 1994 IEEE Medical Imaging Conference (Norfolk, VA)*, Nov. 1994, (in press).

[13] S. S. Barbour, R. L. Barbour, P. C. Koo, J. Chang, H. L. Graber, "Mapping of photon distributions and imaging of MR–derived anatomically accurate optical models of the female breast," accompanying paper in these proceedings.

[14] M. H. Kalos, P. A. Whitlock, *Monte Carlo Methods*, vol. I, John Wiley & Sons, New York, NY, 1986.

[15] H. C. van de Hulst, *Multiple Light Scattering: Tables, Formulas, and Applications*, vol. 1, Academic Press, New York, NY, 1980.

[16] B. B. Das, J. Dolne, R. L. Barbour, H. L. Graber, J. Chang, F. Liu, R. R. Alfano, "Recognition of opaque phantoms and finite absorbers in diffusive media from time–resolved data using tomographic image reconstruction," accompanying paper in these proceedings.

[17] H. L. Graber, R. L. Barbour, J. Chang, R. Aronson, "Identification of the functional form of nonlinear effects of localized finite absorption in a diffusing medium," accompanying paper in these proceedings.